Version of Record: https://www.sciencedirect.com/science/article/pii/S152661252200891X
Manuscript_387ec6a1a2a50dbba744ae9d4dccc7ce

Mechanical Behavior of Bimetallic Stainless Steel and Gray Cast Iron Repairs via Directed Energy Deposition Additive Manufacturing

Jakob D. Hamilton[a], Samantha Sorondo[a], Beiwen Li[b], Hantang Qin[c], Iris V. Rivero[a]

[a] Department of Industrial and Systems Engineering, Rochester Institute of Technology, One Lomb Memorial Drive, Rochester, NY 14623
[b] Mechanical Engineering Department, Iowa State University, 2529 Union Drive, Ames, IA 50011
[c] Department of Industrial and Manufacturing Systems Engineering, Iowa State University, 2529 Union Drive, Ames, IA 50011

Corresponding Author: Iris V. Rivero, iris.rivero@rit.edu, One Lomb Memorial Drive, Rochester Institute of Technology, Rochester, NY 14623

Highlights

- Directed energy deposition of stainless steel 316L restored the strength of cast iron specimens
- Mechanical behavior of repairs remains sensitive to deposition parameters and thermal cycle
- Brittle metastable microstructures and solidification stresses contribute to premature failure
- Gas generation and escapement are visible using in-situ high speed melt pool imaging

Keywords: additive manufacturing, repair, directed energy deposition

Abstract

The utility of gray cast iron in engine components remains tied to the mechanical performance and cost. Repair and remanufacturing of castings offer economical and sustainable benefits; however, high thermal input from traditional fusion-based welding is unable to restore the original mechanical quality owing to brittle microstructures and porosity formed in situ. Directed energy deposition (DED) is an additive manufacturing method that has received considerable interest for repairs owing to the highly controllable nature of the process. Despite this, few works have connected the effect of DED parameters on actual interfacial strength. Consequently, distinct DED parameter combinations were identified to maximize the strength and fatigue life of the repaired cast iron. High speed melt pool imaging and residual stress measurements are provided to aid in the understanding of the metallurgical quality and strength seen in

Abbreviations
GCI – Gray Cast Iron
TC – Temperature Controlled
SS316L – Stainless Steel 316L

these structures. In general, higher scanning speeds and lower thermal gradients promoted comparable tensile strength to that of the original gray cast iron. The results presented here provide a foundation to tune in the DED process to generate the required mechanical quality as a starting point for future process advancements.

1. Introduction

Gray cast iron is a widely used iron alloy in the automotive and transportation industries. Owing to its high strength and wear resistance, gray cast iron can withstand harsh conditions of engine blocks, mechanical housings, and other large components. Because of the high production costs, repairing or remanufacturing large cast iron components is often advantageous.

Cast iron repair commonly employs oxyacetylene or arc welding with mild steel, cast iron, stainless steel, or nickel alloy filler metal [1–3]. Under careful control, these materials allow for restoration of the original material strength. However, achieving this behavior requires overcoming several major challenges. The rapid melting and solidification promoted by welding forms large thermal gradients and brittle martensite in the heat affected zone (HAZ). Residual stresses driven by the large thermal gradients often result in undetectable fractures at the repair interface [1,2]. Controlling these outcomes requires careful control of the cooling rates in-process [4,5]. Gaseous porosity may also form during fusion-based repairs, further decreasing the mechanical integrity of the repair.

Directed energy deposition (DED) is an additive manufacturing technology that has recently been investigated as an alternative repair technology to welding. Lower heat input in laser-based DED has been offered as an advantage to minimize the thermal gradients and the size of the HAZ [6]. Despite this, micro-fracturing and pore formation at the repair interface deteriorate the repair strength. These defects are driven by the unique thermal conditions promoted in DED and can vary significantly with the selected deposition parameters.

Several studies have been offered to understand how distinct deposition parameters affect the interfacial characteristics of the repair [7–11]. Volatile compounds in the cast iron and trapped carrier gas contributed to microporosity in Ni-based alloy coatings on ductile and gray cast iron [9]. Ocelík et al. provided three recommendations for minimizing gas and inter-run porosity in coatings on cast iron: retain dilution between 5-15%, retain a 100 degree angle between the cladding sidewall and the substrate, and minimize the amount of shielding gas [7]. Tong et al. added that the lengthened molten state created by slower scanning speeds allowed trapped gases to escape [8]. The reduced porosity contributed to the improved thermal fatigue resistance in the samples [8]. Other authors have utilized laser remelting to remove porosity in samples, however, the outcomes remain sensitive to laser processing parameters [12]. Li et al. observed that only one of four cladding process parameter sets prevented interfacial porosity in FeNiCr alloy cladded on nodular cast iron [13]. The interfacial porosity caused a notable decrease in the tensile strength of DED-repaired cast iron samples [13].

Interfacial fracturing also remains a significant problem in fusion-based repair of cast iron. The brittle cast iron phases formed through rapid solidification are particularly prone to fracturing when subjected to solidification stresses. Li et al. investigated crack propensity from varying power input while depositing Ni-Cu on nodular cast iron [14]. Excessive power produced chilled ledeburite structures around graphite nodules which acted as fracture initiation points. Insufficient laser power resulted in lack-of-fusion voids which also initiated fracture. Lee et al. reported that excess carbon and silicon near the interface of DED-repaired medium carbon steel contributed to cracking in the first layer of the repair [15]. Reducing the dilution into the substrate was offered as a solution to minimize the influence of carbon. Weng et al. recommended minimizing laser input to reduce graphite dissolution and the resulting ledeburite formation in ductile cast iron [16]. The authors also noted that less heat input would reduce residual stresses and solidification cracking [16]. Yet, residual stress magnitudes for different process conditions remain underreported.

Despite the prevalence of micro-cracking and porosity, few works have quantified the resultant material strength of DED repaired cast iron. While the connection between process parameters and micro- and macro-structural characteristics has been studied, few works have attempted to bridge process parameters and resultant structural characteristics to the interfacial strength of the repair [11,13,14]. This work aims to detail the mechanical behavior of DED-repaired gray cast iron in the context of the residual stresses, porosity, and microstructures formed in the fusion process under different temperature conditions. In-situ substrate temperature control is employed to minimize the thermal gradients during deposition and minimize martensitic formation at the repair interface. In addition to mechanical testing, nondestructive residual stress measurements are also presented to compare the thermal stresses generated by select deposition conditions. By controlling the thermal fields promoted in DED, deleterious material characteristics (porosity, micro-fractures, and more) may be minimized.

2. Methodology

2.1 Experimental Setup

A 5-axis CNC machine retrofitted with a Hybrid Manufacturing Technologies (Dallas, TX, USA) AMBIT tool was used in the printing process (Figure 1). The DED system operates an IPG Photonics (Oxford, MA, USA) Yb-doped fiber laser (λ=1070 nm, Gaussian intensity distribution) with a maximum output of 2 kW. Powder and argon shielding gas are fed coaxially, and the laser spot melts the powder to form a track. Gas atomized stainless steel 316L (SS316L) powder (d_{10}=49 µm, d_{50}=61 µm, d_{90}=92 µm) was deposited on gray cast iron (GCI) plates (ASTM A48 Class 40). Fe-Ni-Cr alloys such as stainless steel are commonly used as filler materials in cast iron repair due to their excellent weldability [10,11,13,17] Supplier chemical compositions of these materials can be found in Table 1.

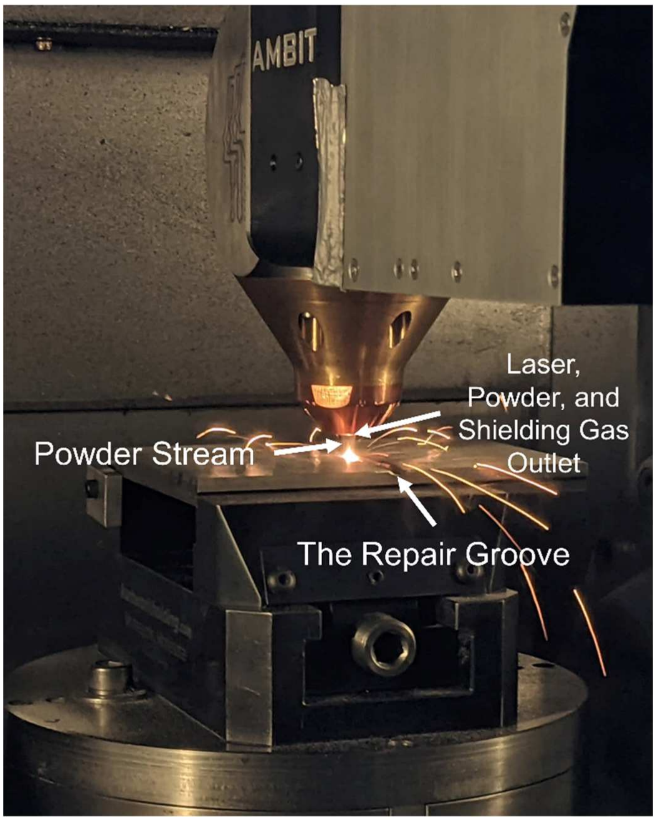

Figure 1. The Hybrid DED system used during experiments.

Material	**C**	**Cr**	**Cu**	**Fe**	**Mn**	**Mo**	**N**	**Ni**	**O**	**P**	**S**	**Si**	**Sn**
GCI plate	3.12	-	0.38	bal.	0.71	-	-	-	-	0.15	0.09	2.20	0.05
SS316L	0.01	17.0	<0.01	bal.	0.80	2.3	0.2	12.1	0.03	<0.005	0.004	0.45	-

Table 1. Chemical composition (wt%) for the substrate and powder used in the experiment.

The cast iron substrates were machined to 140 mm × 100 mm × 12.7 mm. A 2 mm deep trapezoidal groove with 45° walls was machined along the centerline of the part such that five subsize tensile bars could be machined transverse to the groove length. Subsize tensile specimens were ground to a thickness of 2 mm. Drawings of the substrate and tensile bar locations are shown in Figure 2.

An in-situ heating setup was constructed to be able to control the temperature of the substrate during deposition. The setup consisted of two 300W resistive heaters attached to the underside of the substrate via bolts and a thermocouple inserted 25.4 mm into the cast iron plate for monitoring temperature. An image of the thermocouple location is included in Figure 2. A temperature controller utilized real-time thermocouple data to maintain the substrate at 300°C during the print and during cooldown. This temperature has been previously identified as ideal for cast iron repair [3,4].

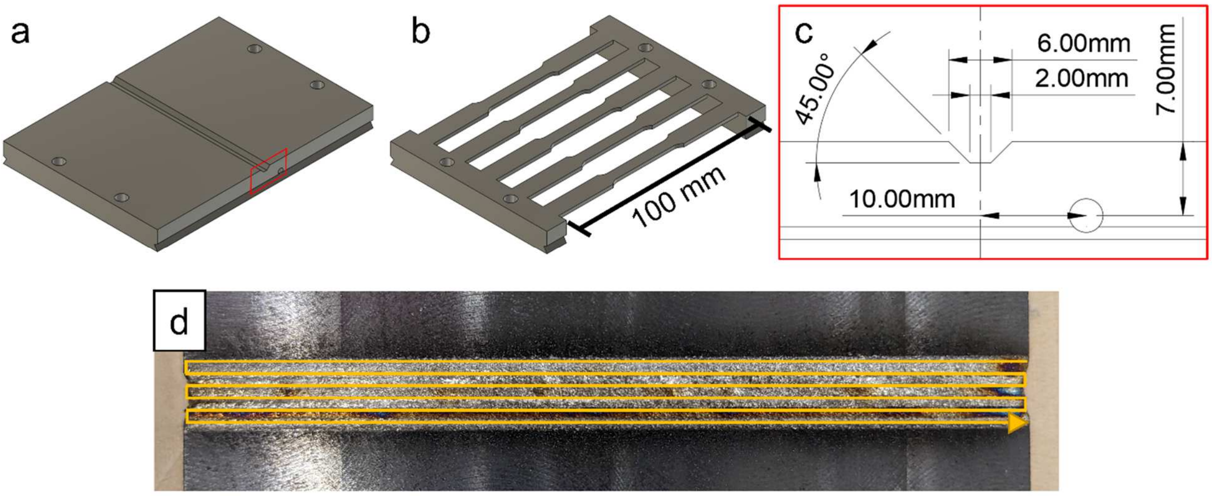

Figure 2. The groove repair samples (a) before repair and (b) after repair and post process machining. (c) The groove dimensions and thermocouple insertion location. (d) The repair pattern on the final layer of the samples.

2.2 Experiment

The groove repair was completed by depositing stainless steel in four layers to completely fill the void. Each layer consisted of tracks of alternating directions along the groove length. An additional laser pass was added at each layer such that the first layer was filled using 3 tracks, the second layer with 4 tracks, and so on.

To investigate the effect of distinct thermal conditions on the mechanical properties, in-situ heating and scanning speed were varied. For thermally controlled (TC) samples, the substrates were preheated to and held at 300°C during the print. After finishing the repair, the TC samples were annealed at 300°C for 2 hours after printing. Because of the additional energy input in TC samples, laser power was lowered by 25%. This value was selected for its excellent melt pool stability in prior experiments. Grooves were repaired with laser scanning speeds of 350 mm/min, 500 mm/min, and 650 mm/min. Powder mass flow rate was adjusted for each sample such that the ratio of powder mass flow rate to laser scanning speed was constant at 9.3 g/m. A full two-factor factorial was used for the experimental design with TC mode and scanning speed as factors. The deposition parameters held constant across samples are shown in Table 2. Identical tensile bars from the untreated GCI were used as control samples.

Parameter	Value	Unit	Parameter	Value	Unit
Laser power (non-TC)	1033	Watts	Laser spot diameter	2.4	mm
Laser power (TC)	750	Watts	Carrier gas flow rate	3	L/min
Stepover	1.2	mm	Shield gas flow rate	5	L/min
Nominal layer height	0.75	mm	Nozzle gas flow rate	10	L/min

Table 2. Parameters for the DED repair operations.

2.3 Characterization

In-situ melt pool images were captured by an Edgertronic (San Jose, CA, USA) SC2+ high-speed camera. The camera was mounted off-axis at a 45° vertical angle toward the substrate surface normal. A 1070 nm notch filter was placed in front of the lens to shield the camera from excess laser intensity. Camera parameters remained constant between comparisons to retain equivalent exposure. Images were captured at 2,500 frames per second.

Residual stresses were measured on the surface of the as-printed and as-machined groove repair in longitudinal and transverse directions above each of the tensile bar locations. These are the primary directions in which residual stresses typically develop in welding [18]. Longitudinal stresses refer to the stresses oriented parallel to the groove length, and transverse stresses refer to the stresses oriented parallel to the tensile bars. A Proto Manufacturing (Taylor, MI, USA) mXRD Residual Stress Analyzer gathered nondestructive x-ray diffraction residual stress measurements via the $\sin^2\psi$ method according to ASTM E2860 [19]. Mn-Kα x-rays (λ=2.1031 Å) were exposed 20 times at 11 incident (β) angles for 2.5 seconds per exposure. This results in 22 ψ-angle tilts in the resulting stress calculation. The Bragg angle (2θ) used in measurement was 152.8°, the “311” austenitic phase. X-rays were generated at 18.1 kV and 1.8 mA. A 1.0 mm round aperture was utilized, and the sample was oscillated 3.0 mm in the X- and Y-directions and 3.0° in the β-direction. This was done to increase the number of grains sampled and avoid effects from preferred grain orientation [20]. The x-ray elastic constants used were ½(S_2) = 7.18E-6 MPa^{-1} and –(S_1) = 1.20E-6 MPa^{-1}. These are derived from the Young's Modulus and Poisson's Ratio of bulk austenitic stainless steel and were provided in the Proto Manufacturing software.

Tensile testing was performed on two ground samples of each treatment combination. The testing was based in subsize tensile testing described in ASTM E8 [21]. Samples were pulled at 2.0 mm/min using a 5,000 lb. load cell. Strain was taken from the crosshead displacement. Fatigue testing was performed in incremental steps of 1,000 cycles to account for the large range of ultimate tensile stresses (UTS) expected in the samples. Since UTS values from tensile testing exhibited a large standard deviation, results were corroborated by performing incremental-step fatigue testing. This methodology encompassed the broad range of fatigue strength values by having the average fatigue stress magnitude of each sample coincide with half of the average UTS values of each sample. This fatigue test was based on a modified version of Nicholas' methodology [22]. Other versions of the step fatigue testing technique have been used to test components produced via additive manufacturing [23–25]. The fatigue life of tensile samples was measured up to failure with a stress ratio of R=0.5 and 0.5 Hz frequency.

Porosity analysis of unbroken tensile specimens was conducted using computed tomography. Two samples were scanned for porosity analysis: 500 mm/min with and without TC. Pore thresholding was conducted using Volume Graphics Studio MAX (Heidelberg, Germany). Filtering was applied to distinguish pores from fractures. Cross sections of fractured tensile samples were mounted, ground, and polished for metallographic analysis. Polished samples were etched for 7 seconds using nitric acid (3 vol%) in ethanol (97 vol%). Vickers microhardness was taken with a 200 g load and 10 s dwell at 5 locations across the SS316L and GCI interface (Figure 3).

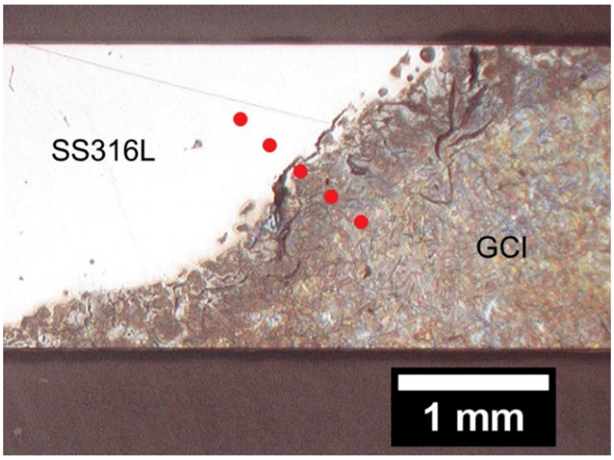

Figure 3. Approximate locations for microhardness measurements on a tensile bar cross section.

3. Results

3.1 Residual Stresses

Figure 4 shows the residual stresses at the center of the groove repair sample for each of the scanning speeds in TC samples. The stresses are shown on the as-printed surface and after the surface was machined flat to the substrate surface. For the as-printed samples, residual stresses were tensile between 0 MPa and 150 MPa and were higher in the longitudinal directions, i.e., oriented parallel to the scanning direction. On the machined surface, residual stresses were highly tensile between 500 MPa and 650 MPa. Transverse stresses were higher than longitudinal stresses on these surfaces. The face-milling operation likely creates high shearing stresses that create the high tensile stresses [26].

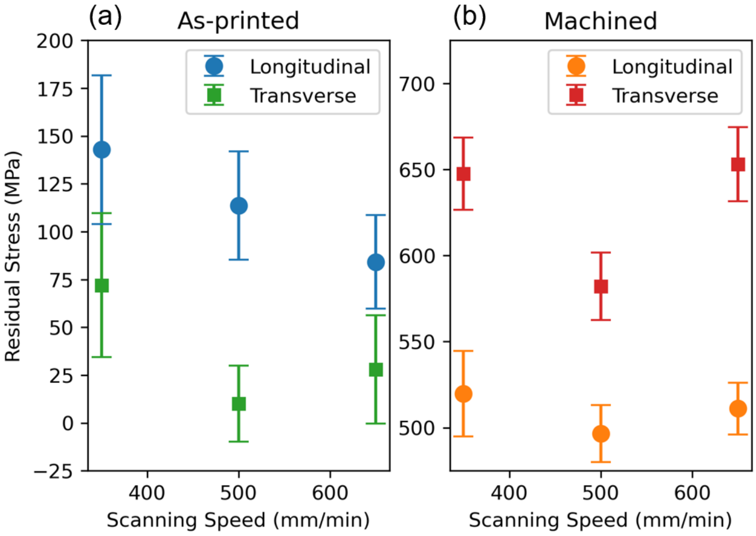

Figure 4. (a) As-printed and (b) machined RS at the center location in TC groove repair samples as a function of scanning speed.

The residual stresses across the as-printed groove repair are shown in Figure 5. This data includes stresses for different scanning speeds and with and without TC. Longitudinal stresses were tensile between 20 MPa and 220 MPa. The transverse stresses were either compressive up to 150 MPa or tensile up to 110 MPa. The longitudinal residual stresses were similar between TC and non-TC conditions across the entire groove length. Excessive surface roughness at the 350 mm/min contributed to inconsistent residual stress measurements in the longitudinal direction. Transverse residual stresses were also similar between TC and non-TC conditions but showed distinct patterns for each scanning speed condition. For the 350 mm/min condition, stresses at the center of the sample were higher than those toward the ends of the grooves. The 650 mm/min condition showed tensile stresses at one end of the groove and transitioned to compressive stresses near the other end of the sample.

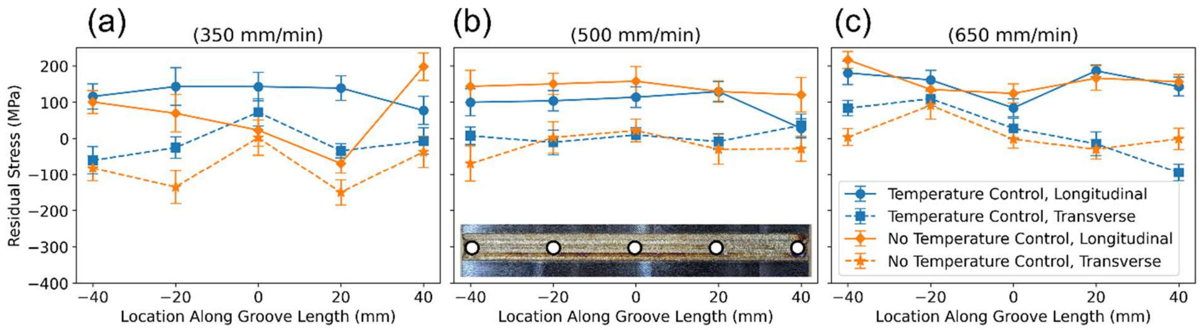

Figure 5. As-printed residual stresses in the (a) 350 mm/min, (b) 500 mm/min, and (c) 650 mm/min samples with and without in-situ temperature control. (b) shows the explicit measurement location on the samples.

3.2 Interfacial Strength

Interfacial strength appeared to vary depending on the printing parameters selected for the repair operation (Figure 6). Faster scanning speeds generally improved the strength of the deposited material. In both the TC and non-TC conditions, samples printed at 650 mm/min showed considerably higher tensile strength than 500 mm/min and 350 mm/min samples. Similarly, employing temperature control during and after the printing process improved the strength of the material. The highest-strength process parameters from the studied conditions, 650 mm/min with TC, promoted comparable ultimate tensile strength to the GCI despite yielding at lower stresses than the GCI. The 500 mm/min sample with TC showed comparable stiffness to the control samples but retained around 50% of the original material strength. Conversely, the lowest strength was observed in the 350 mm/min without TC. These samples failed during testing prior to any meaningful data being collected.

As for fracture locations, almost all repair samples fractured immediately outside of the interface between the GCI plate and SS316L deposition. The GCI control samples broke outside the gauge region. In one 650 mm/min sample repaired with TC, the fracture occurred wholly in the GCI outside of the gauge region rather than at interface. This indicated the strength of the repaired interface in this sample was higher than that of the surrounding GCI.

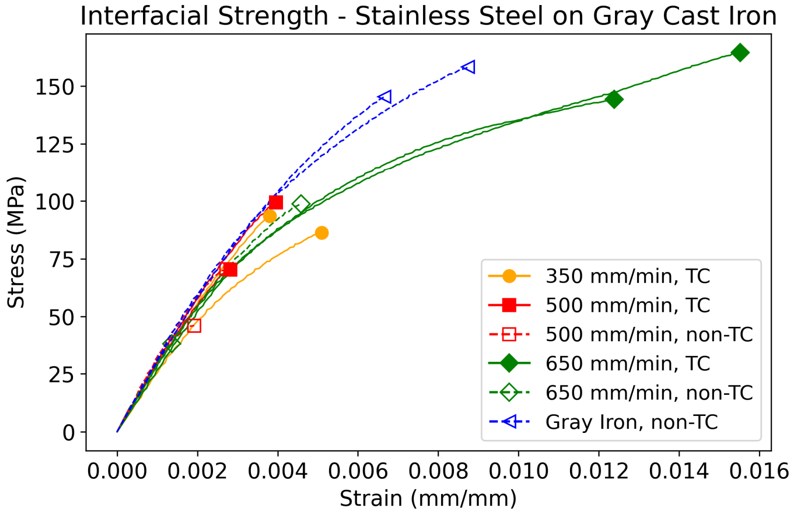

Figure 6. Interface strength of the repaired cast iron for a variety of deposition conditions.

3.3 Fatigue Life

As with the tensile tests, the non-TC samples showed lower strength compared to TC samples (Figure 7). Non-TC samples of 350 mm/min and 500 mm/min broke prior to data being collected, indicating poor repair quality. Sample fractures primarily occurred at the repair interface, likely the result of high martensite concentrations in the HAZ. The 650 mm/min TC samples performed comparably to the grey cast iron sample, indicating the original strength was restored using these conditions. From these results, it can be observed that temperature control and scanning speed are determining factors in the repair strength.

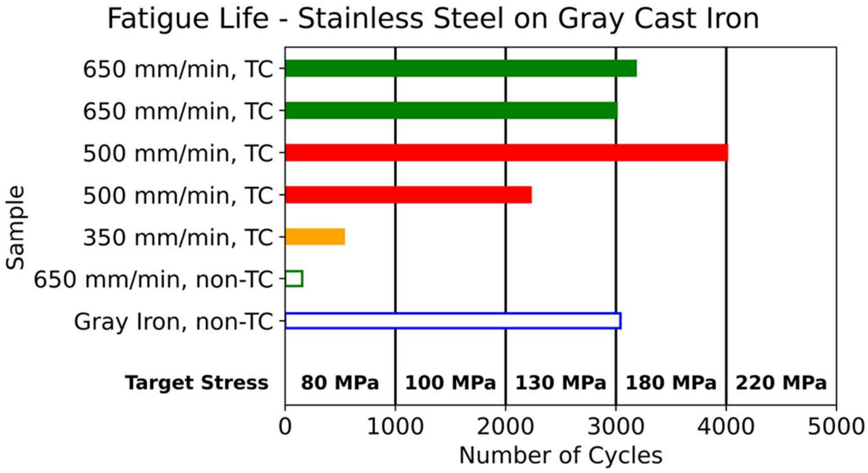

Figure 7. Fatigue life as a function of the target stress during each step and the number of cycles.

3.4 Macrostructural Defects

Samples showed varying levels of gas generated porosity, apparent by the round morphology of the pores (Figure 8). In non-TC samples, the slower 350 mm/min and 500 mm/min scanning speeds promoted higher levels of gas-trapped porosity. Pores were between 250-750 µm in size. As scanning speed increased to 650 mm/min, only smaller (100-200 µm) pores were visible along the interfacial region in the cross section images. In the TC condition, fewer pores were noted and were most prevalent along the GCI-SS316L interface. Like non-TC samples, pores were less frequent at higher scanning speeds. Computed tomography confirmed these findings within 500 mm/min samples (Figure 9). Large (>500 µm) spherical pores formed in non-TC samples, and in several cases, pores agglomerated into clusters as large as 1.4 mm. The location of these clusters suggests that remelting of the first layer combines smaller gas-generated pores into large pores and relocates these into subsequent layers. TC samples generally did not exhibit this behavior; pores were primarily small and located along the bimetallic interface. Further studies are needed to decouple the pore size and location behavior from the chosen TC cycle and the selected process parameters.

Micro-cracking was also observed in two locations in non-TC and TC samples: along the bimetallic interface and within the deposited stainless steel. The former is obvious in the tensile cross sections in Figure 8. Fractures within the stainless steel showed varying sizes. The 500 mm/min TC sample showed fractures 20-50 µm wide and up to 5 mm long within the first deposited layer (Figure 9(d)). Without temperature control, these fractures were nearly twice as wide and propagated through the first two layers of the sample (Figure 9(b)). These fractures are characteristic of cast iron repair and are caused by the tensile stresses formed in the process [1]. The lower thermal gradient from preheating and lengthened cooling allowed first-layer residual stresses to relax and suppress excessive fracturing. Further suppression of fusion zone fractures could be accomplished with a high-ductility filler material such as nickel-based alloys albeit at a higher material cost.

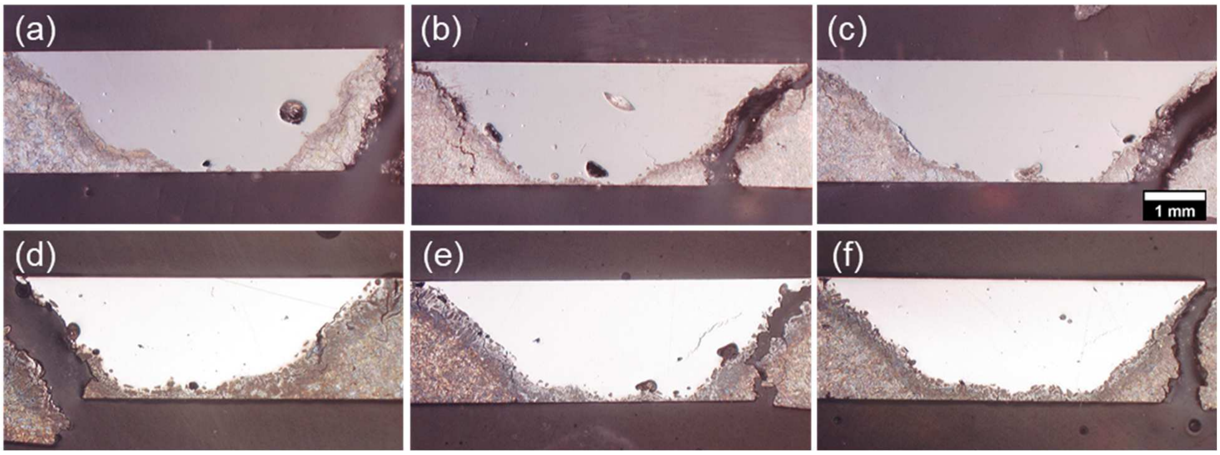

Figure 8. Cross sections of non-TC samples at (a) 350 mm/min, (b) 500 mm/min, and (c) 650 mm/min and TC samples at (d) 350 mm/min, (e) 500 mm/min, and (f) 650 mm/min.

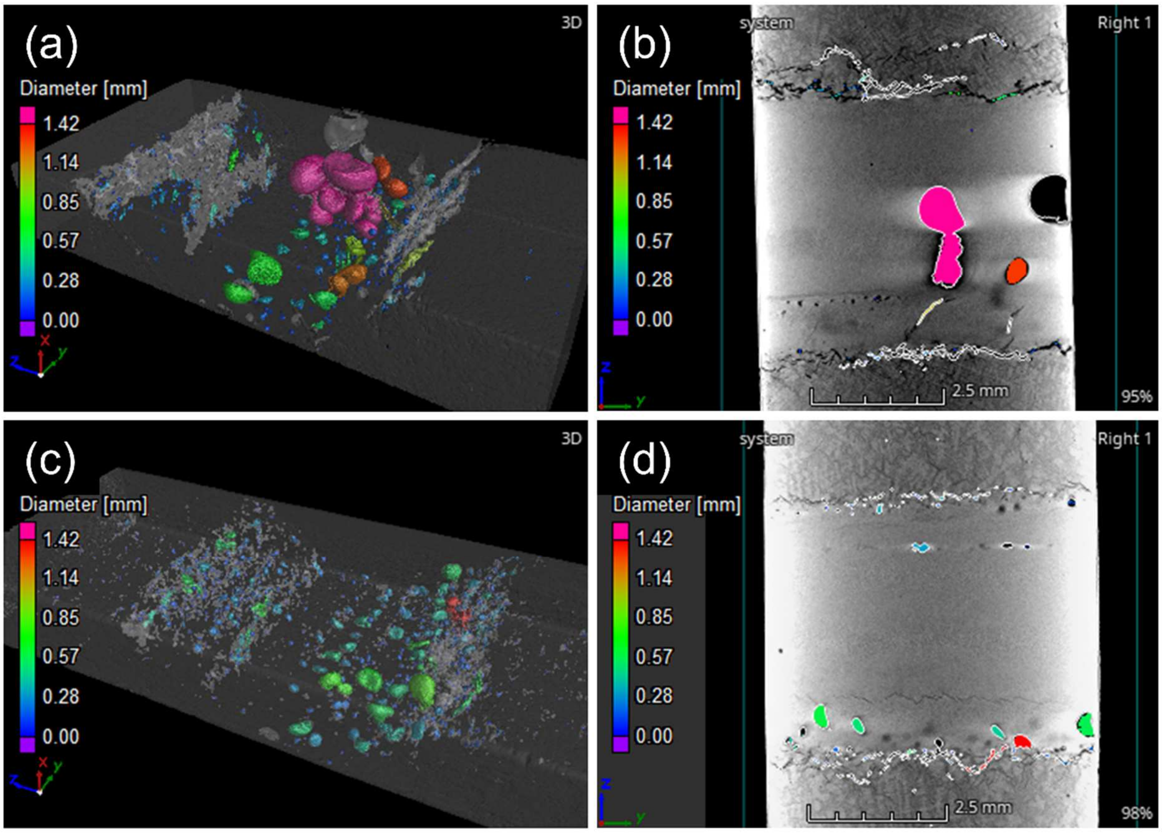

Figure 9. Internal porosity and micro-cracking observed via computed tomography in (a, b) 500 mm/min non-TC and (c, d) 500 mm/min TC samples.

Pore formation was studied in situ using high-speed melt pool imaging. Figure 10 shows frames from 350 mm/min, 500 mm/min, and 650 mm/min single-track depositions on non-TC cast iron. At 350 mm/min, the melt pool is observed to grow and collapse several times per second. This behavior is less frequent in the 500 mm/min sample and even less so in the 650 mm/min sample. The melt pool morphology remains relatively consistent at 650 mm/min. The bubbling seen at lower speeds is likely gas escaping the melt pool. A combination of trapped gas and the liquid turbulence following a collapse event contributes to the higher porosity at lower scanning speeds. The gas escapement phenomenon was not noted in high-speed images of TC samples. The increased melt pool stability in TC samples could be attributed to the thermal conditions or the decreased laser power. Figure 11 shows high-speed imaging of 500 mm/min samples repaired at 750 W laser power with and without TC. In both cases, the melt pool showed high stability with infrequent gas escapement. The melt pool was also considerably smaller compared to the samples repaired with 1033 W laser power. These results signal that preheating does not alleviate gas formation in DED-based repair of cast iron. Instead, the dilution caused by localized melting is the dominant factor in gas generation and melt pool stability.

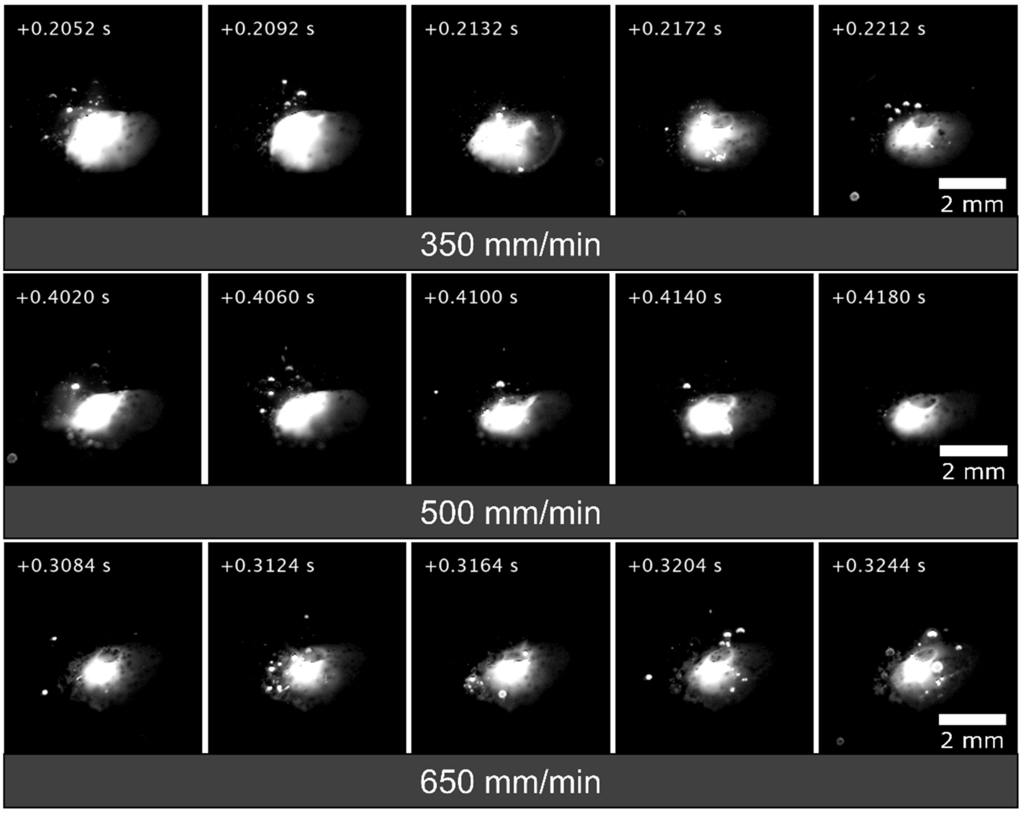

Figure 10. High-speed melt pool images of 350 mm/min and 650 mm/min single tracks deposited on GCI. Accompanying videos are included as supplementary data.

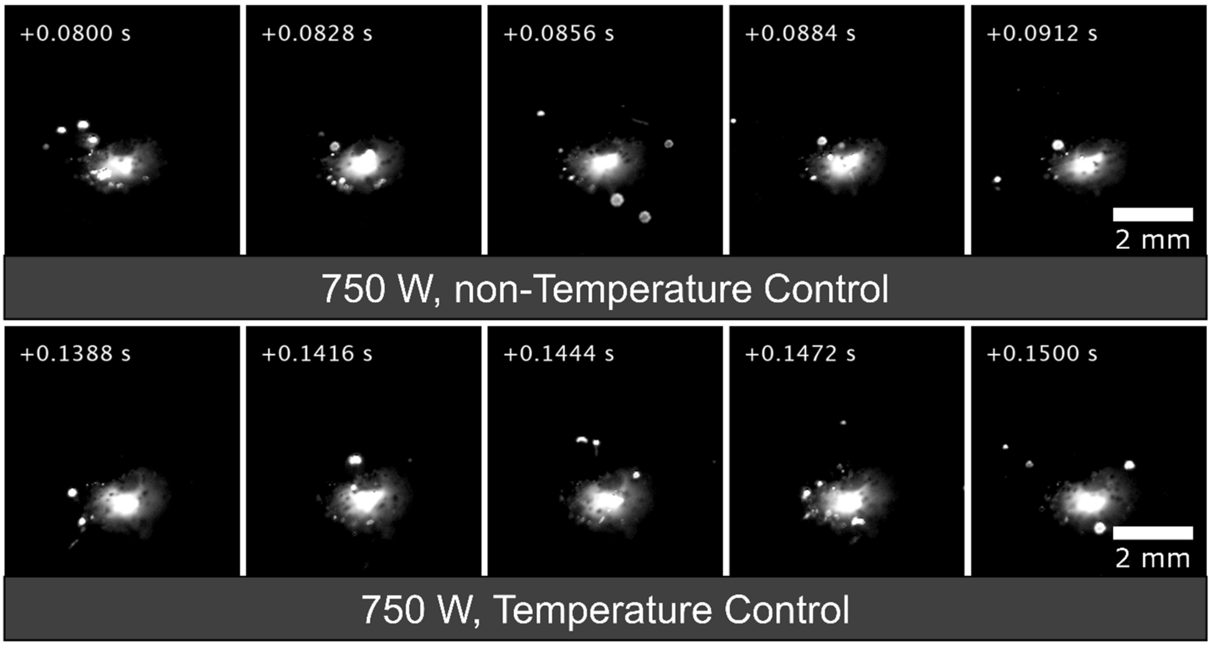

Figure 11. High-speed melt pool images of 750 W, 500 mm/min single tracks deposited on GCI with and without TC. Accompanying videos are included as supplementary data.

3.5 Microstructure and Microhardness

The microstructures in repaired samples showed distinct regions of (1) monolithic stainless steel, (2) a partially melted zone (PMZ) with combined stainless steel and cast iron, (3) a heat affected zone (HAZ) of iron-carbon alloys and graphite, and (4) unaffected pearlitic cast iron (Figure 12). During cladding, the melt pool reached temperatures sufficient to melt up to 200 µm below the substrate, generating the PMZ. The HAZ immediately surrounds this region up to 250 µm in depth for non-TC samples and 440 µm for TC samples. The PMZ featured graphite flakes surrounded by martensite and ledeburite. Non-TC samples exhibited martensite throughout the HAZ, indicative of the rapid cooling from fusion. The lower heat input and annealing condition of the TC samples suppressed martensite formation in the HAZ, limiting the martensite and ledeburite solely to the PMZ. These metastable phases are typically detrimental to the interfacial strength due to their brittle nature but are difficult to avoid during fusion-based cast iron repair [13,27,28]. Suppression of these phases in TC samples is likely the driving factor for the excellent tensile strength compared to non-TC samples.

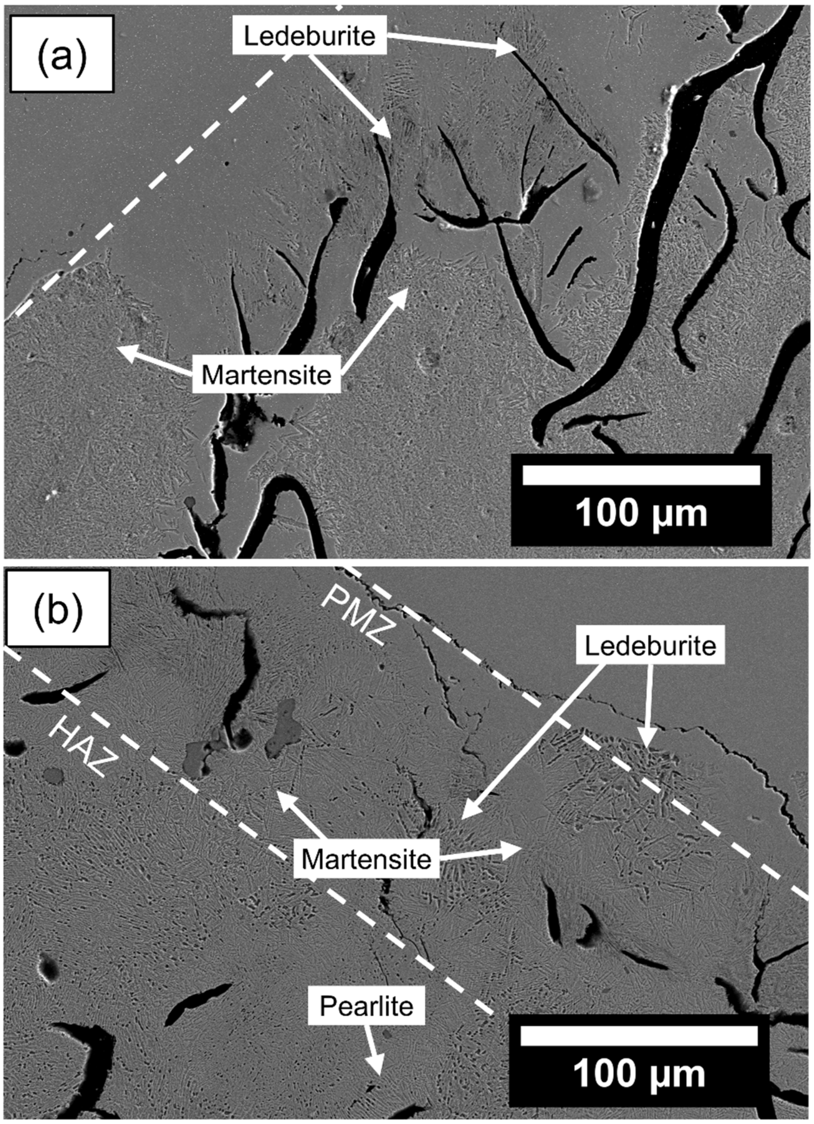

Figure 12. SEM images of fractured tensile bar cross sections for 650 mm/min (a) non-TC and (b) TC samples.

In several samples, the PMZ featured discrete regions of iron-carbon alloy surrounded by stainless steel. These are observed as the darker "islands" in the backscattered electron composition images in Figure 13(a, b). Additional imaging revealed these regions as metastable formations of iron and carbon (Figure 13(c)). Similar regions are observed in other studies of laser cladding on cast iron [6,12,13]. It is likely that Marangoni convection within the melt pool mixed the carbon-saturated base material with the deposited stainless steel. Because of the high solidification rate, the carbon likely did not have sufficient time to diffuse into the surrounding material and formed islands of carbon-rich ledeburite and martensite seen along the interface. Martensite was evident from the needle-like acicular subgrains (Figure 13(d), while ledeburite was visible as the light and dark phase striations surrounding graphite flakes (Figure 13(e)). These regions are also more prevalent in slower scanning speed samples. The slower solidification front at these speeds increases the duration of Marangoni convection at any given location, thus incorporating more carbon-rich iron into the melt pool. Because these regions are unable to diffuse carbon to the surrounding stainless steel, ledeburite and martensite form. The presence of these "islands" is likely not the sole detriment to the mechanical strength; however, the increased volume of these phases contributes to the poor tensile behavior.

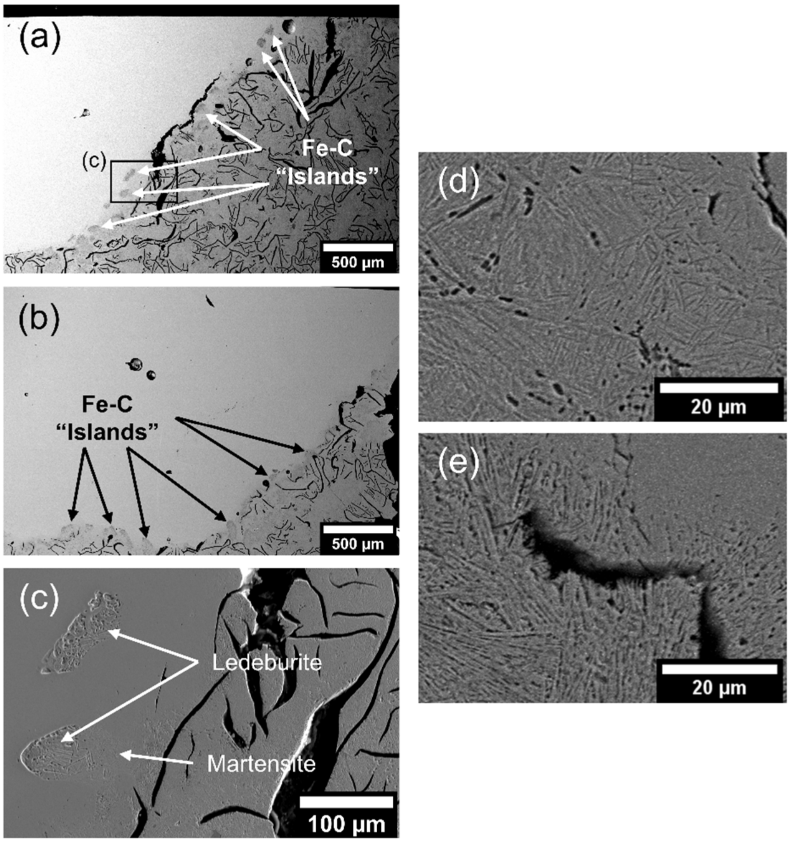

Figure 13. Discrete islands of metastable Fe-C in the partially melted zone for samples (a) 350 mm/min TC and (b) 650 mm/min TC. (c) shows the boxed region in (a) in higher detail, noting martensite (d) and ledeburite (e).

The measured microhardness values are compared in Figure 14. The microhardness distributions across the repair were consistent with previous literature [13,29]. The SS316L exhibited microhardness between 200-300 HV, slightly higher than other additively-manufactured SS316L studies [30,31]. For the cast iron, the microhardness was highest at the interface (300-600 HV) and decreased farther from the heat-affected zone (250-400 HV) due to the varying microstructures formed in-process. The cementite and ferrite comprising the pearlitic steel far from the interface are lower strength phases compared to martensitic steel [32]. No clear trends were apparent between scanning speed levels, despite showing considerable differences in tensile behavior. This points to the differences between micro- and macro-level strength measurements. Although samples show similar microhardness behavior around the interface, this measurement does not capture the differences in interfacial strength.

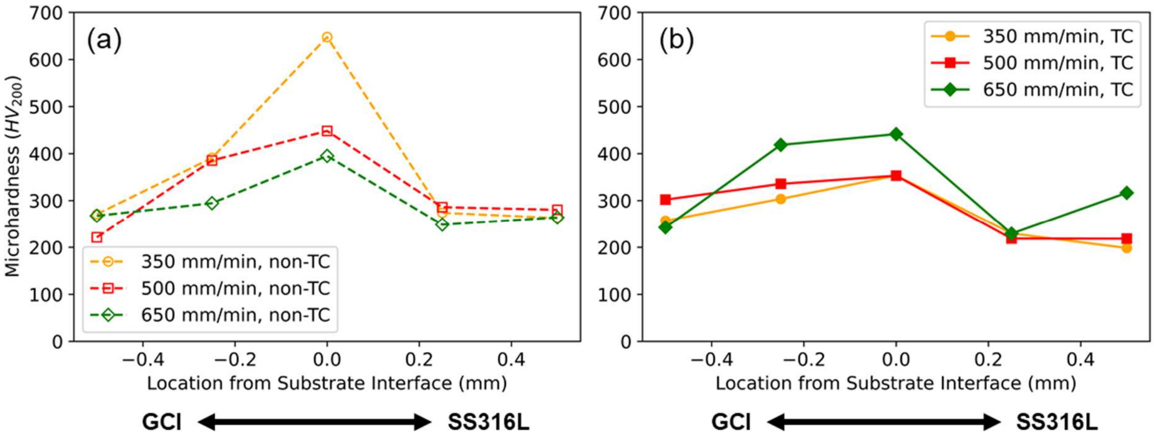

Figure 14. Microhardness across the interface for (a) non-TC and (b) TC samples.

4.0 Discussion

The key observation in these results is the effect of DED processing on the formation of defects and brittle phases of cast iron and the resultant mechanical behavior. The degree of pore formation appears highly dependent on the applied thermal field with higher temperatures providing higher dilution and higher rates of gas-generated porosity. The former conclusion is supported by the dilution and porosity seen in optical microscopy and computed tomography, while the latter is supported by in-situ high speed imaging. While the direct effect of porosity on the resultant mechanical behavior is difficult to decouple from microstructural effects, the suppression of porosity in TC samples contributed to improved tensile and fatigue behavior. The exact mechanism for pore formation in DED repair of cast iron remains in question. Arias-González et al., for example, attributed micro-porosity formed in Ni-alloy coatings on cast iron to either 1) injection of the carrier gas into the melt pool, or 2) volatile compounds reacting in process [9]. Dass and Moridi supported the latter notion that the combination of metal vaporization and inert gas shielding contributes to gas entrapment [33]. Moisture contamination of the powder feedstock may also be a driving factor for gas generation in DED [34]. Previous work in selective laser melting has attributed trapped gas porosity to the nonequilibrium and unstable convection flow caused by excess energy input [35,36]. High energy input increases dilution and likely drives the rate of vaporization during processing, supporting the notion by Dass and Moridi [33]. Figure 10 and Figure 11 indicate the rate of gas generation and escapement is dependent on DED process parameters. Process parameters that promote higher dilution, i.e., slower scanning speeds and higher laser power, encourage higher melt pool gas generation. Work from Zhang et al. and Gong et al. support this notion that the melt pool instability and porosity is caused by high energy input [35,36]. The use of cast iron as a substrate offers another explanation, however. Figure 15 compares the transient melt pool behavior for identical deposition conditions on cast iron and mild steel (0.2% carbon). In these images, cladding on cast iron showed frequent gas escapement and melt pool instability. Conversely, cladding on mild steel showed stable melt conditions and no obvious gas escapement events. This suggests that the gas generated from depositing on cast iron is likely CO and CO_2 gases produced from ambient oxygen reacting with graphite. In combination with Figure 10 and Figure 11, these results indicate that gas generation in DED cast iron repair is a function of the dilution, energy input, and the amount of carbon present in the cladding surface. In the absence of post-processing strategies such as hot isostatic pressing, in-envelope porosity reduction strategies should be developed to reduce the amount of carbon present on the cladding surface. Likewise, this method of in-situ high speed melt pool imaging could be incorporated into a feedback system to tailor the incident laser power to control melt pool stability and further mitigate porosity.

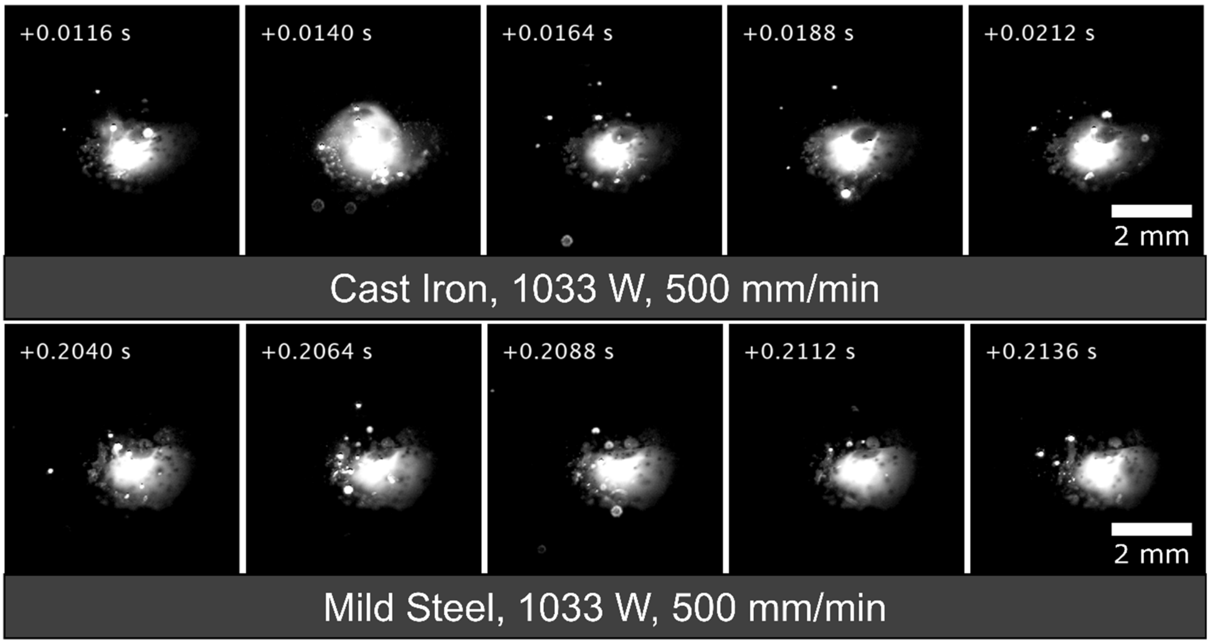

Figure 15. Laser cladding (Power=1033W, Scanning speed=500 mm/min) on cast iron and mild steel. The transient melt pool behavior during laser cladding on cast iron is indicative of porosity in the final structure. Accompanying videos are included as supplementary data.

The degree of solidification cracking is also a key determinant in mechanical behavior. In welding, the use of preheating and annealing served to minimize the thermal gradient and suppress residual stresses that form fractures [18]. Slow cooling also serves to suppress the formation of brittle phases [18]. The formation of these phases in DED-based cast iron repair has been described previously, although the resultant effect on fatigue behavior of the interface is scarcely reported [27]. Although martensite and ledeburite are high strength phases, the brittle nature of these phases significantly reduces the integrity of the repair. This is evident from the interfacial strength results observed herein: samples with higher heat input and large spatial and temporal thermal gradients, i.e., non-TC and slower scanning speeds, performed poorly during tensile and fatigue testing. Evaluating the microstructure confirmed that the volume of brittle phases was increased with slower scanning speeds and without TC. These results confirm findings from Yu et al. and their comparative study on welding and DED for repairing gray cast iron [6]. While not eliminated, the lower thermal input offered by DED minimizes the formation of brittle phases and residual stresses that result in solidification cracking. Likewise, the use of TC allows for carbon to sufficiently diffuse and prevent the formation of brittle phases in the HAZ.

Another aspect to consider in the repair of cast iron is the filler metal. Although SS316L was used for its low cost and machinability, it is well established that nickel and nickel alloys are ideal for cast iron welding. The solubility limit of carbon in nickel is 0.5% at the eutectic temperature, well below that of carbon in iron [1]. This allows for carbon to precipitate as graphite during solidification. Nickel carbide (Ni_3C) is also less stable than iron carbide (Fe_3C) and results in carbon precipitation rather than retention in carbide form [1]. In effect, the brittle cast iron phases are eliminated from the fusion zone and the risk of solidification cracking is minimized. The use of nickel-based filler metal does not, however, eliminate these phases from the PMZ and HAZ. Ledeburite and martensite form in these areas during welding and DED-based processes and are especially notable in absence of preheating [1,14].

5.0 Conclusions

Gray cast iron remains a difficult material to repair owing to the high carbon content within the alloy. Gray cast iron was repaired with stainless steel 316L via different DED processing conditions to unveil relationships between thermal conditions and mechanical properties. Stainless steel 316L offers excellent weldability and is widely available. Many of the defects generated during cast iron repair stem from the high carbon content and rapid solidification present in fusion based processes. The following discoveries were reached:

- Repaired structures demonstrated tensile residual stresses on the surface of repaired structures, indicating the need for repair post-processing to improve fatigue life.
- The combination of low-dilution process parameters, preheating, and annealing minimized the volume of brittle microstructures and solidification fractures around the repair. This resulted in a restoration in the cast iron tensile strength and increased elongation.
- The mechanism for porosity formation was observed to be dependent on thermal conditions. Higher-dilution parameters catalyzed gas formation, pore coalescence, and entrapment in the solidifying melt pool.

The results described within present laser-based DED as a feasible technology for restoring the mechanical strength of worn regions or defects in iron castings due to the highly controllable nature of the process. Successful repairs should utilize preheating and annealing to prevent cracking. The dilution ratio should also be minimized to minimize carbon oxidation while retaining sufficient fusion to the substrate core.

Acknowledgements

The authors would like to thank both the Department of Mechanical Engineering and the Department of Manufacturing and Mechanical Engineering Technology at Rochester Institute of Technology (RIT) for use of their characterization equipment. The authors would like to specifically thank Mark Walluk in the Golisano Institute for Sustainability at RIT for assistance with mechanical testing and Dr. David Trauernicht in the AMPrint Center for assistance with CT analysis.

Funding

This paper is based upon work supported by the U.S. Department of Energy's Office of Energy Efficiency and Renewable Energy (EERE) under the Advanced Manufacturing Office Award Number DE-EE0007897 awarded to the REMADE Institute, a division of Sustainable Manufacturing Innovation Alliance Corp.

Competing Interests

This report was prepared as an account of work sponsored by an agency of the United States Government. Neither the United States Government nor any agency thereof, nor any of their employees, makes any warranty, express or implied, or assumes any legal liability or responsibility for the accuracy, completeness, or usefulness of any information, apparatus, product, or process disclosed, or represents that its use would not infringe privately owned rights. Reference herein to any specific commercial product, process, or service by trade name, trademark, manufacturer, or otherwise does not necessarily

References

[1] M. Pouranvari, On the weldability of grey cast iron using nickel based filler metal, Mater. Des. 31 (2010) 3253–3258. https://doi.org/10.1016/j.matdes.2010.02.034.

[2] F. Malek Ghaini, M. Ebrahimnia, S. Gholizade, Characteristics of cracks in heat affected zone of ductile cast iron in powder welding process, Eng. Fail. Anal. 18 (2011) 47–51. https://doi.org/10.1016/j.engfailanal.2010.08.002.

[3] E.M. El-Banna, M.S. Nageda, M.M. Abo El-Saadat, Study of restoration by welding of pearlitic ductile cast iron, Mater. Lett. 42 (2000) 311–320. https://doi.org/10.1016/S0167-577X(99)00204-9.

[4] E.M. El-Banna, Effect of preheat on welding of ductile cast iron, Mater. Lett. 41 (1999) 20–26. https://doi.org/10.1016/S0167-577X(99)00098-1.

[5] R. Gonzalez, M. Cadenas, R. Fernandez, J.L. Cortizo, E. Rodriguez, Wear behavior of flame sprayed NiCrBSi coating remelted by flame or by laser, Wear. 262 (2007) 301–307. https://doi.org/10.1016/j.wear.2006.05.009.

[6] J.H. Yu, Y.S. Choi, D.S. Shim, S.H. Park, Repairing casting part using laser assisted additive metal-layer deposition and its mechanical properties, Opt. Laser Technol. 106 (2018) 87–93. https://doi.org/10.1016/j.optlastec.2018.04.007.

[7] V. Ocelík, U. de Oliveira, M. de Boer, J.T.M. de Hosson, Thick Co-based coating on cast iron by side laser cladding: Analysis of processing conditions and coating properties, Surf. Coatings Technol. 201 (2007) 5875–5883. https://doi.org/10.1016/j.surfcoat.2006.10.044.

[8] X. Tong, H. Zhou, L. quan Ren, Z. hui Zhang, R. dong Cui, W. Zhang, Thermal fatigue characteristics of gray cast iron with non-smooth surface treated by laser alloying of Cr powder,

Surf. Coatings Technol. 202 (2008) 2527–2534. https://doi.org/10.1016/j.surfcoat.2007.09.014.

[9] F. Arias-González, J. Del Val, R. Comesaña, J. Penide, F. Lusquiños, F. Quintero, A. Riveiro, M. Boutinguiza, J. Pou, Fiber laser cladding of nickel-based alloy on cast iron, Appl. Surf. Sci. 374 (2016) 197–205. https://doi.org/10.1016/j.apsusc.2015.11.023.

[10] J.M. Yellup, Laser cladding using the powder blowing technique, Surf. Coat. Technol. 71 (1995) 121–128. https://doi.org/https://doi.org/10.1016/0257-8972(94)01010-G.

[11] Q. Lai, R. Abrahams, W. Yan, C. Qiu, P. Mutton, A. Paradowska, X. Fang, M. Soodi, X. Wu, Effects of preheating and carbon dilution on material characteristics of laser-cladded hypereutectoid rail steels, Mater. Sci. Eng. A. 712 (2018) 548–563. https://doi.org/10.1016/j.msea.2017.12.003.

[12] Y. Li, S. Dong, S. Yan, X. Liu, E. Li, P. He, B. Xu, Elimination of voids by laser remelting during laser cladding Ni based alloy on gray cast iron, Opt. Laser Technol. 112 (2019) 30–38. https://doi.org/10.1016/j.optlastec.2018.10.055.

[13] Y. Li, S. Dong, P. He, S. Yan, E. Li, X. Liu, B. Xu, Microstructure characteristics and mechanical properties of new-type FeNiCr laser cladding alloy coating on nodular cast iron, J. Mater. Process. Technol. 269 (2019) 163–171. https://doi.org/10.1016/j.jmatprotec.2019.02.010.

[14] Y. Li, X. Liu, S. Dong, X. Ren, S. Yan, B. Xu, Influence of laser power on interface characteristics and cracking behavior during laser remanufacturing of nodular cast iron, Eng. Fail. Anal. 122 (2021) 105226. https://doi.org/10.1016/j.engfailanal.2021.105226.

[15] S. Lee, J. Kim, D.S. Shim, S.H. Park, Y.S. Choi, Micro-Cracking in Medium-Carbon Steel Layers Additively Deposited on Gray Cast Iron Using Directed Energy Deposition, Met. Mater. Int. (2020). https://doi.org/10.1007/s12540-019-00589-5.

[16] Z. Weng, A. Wang, Y. Wang, D. Xiong, H. Tang, Diode laser cladding of Fe-based alloy on ductile cast iron and related interfacial behavior, Surf. Coatings Technol. 286 (2016) 64–71. https://doi.org/10.1016/j.surfcoat.2015.12.031.

[17] Y. Li, S. Dong, S. Yan, E. Li, X. Liu, P. He, B. Xu, Deep pit repairing of nodular cast iron by laser

cladding NiCu/Fe-36Ni low-expansion composite alloy, Mater. Charact. 151 (2019) 273–279. https://doi.org/10.1016/j.matchar.2019.03.021.

[18] S. Kou, Welding Metallurgy, Wiley-Interscience, Hoboken, NJ, 2003.

[19] ASTM International, ASTM E2860-12, Standard Test Method for Residual Stress Measurement by X-Ray Diffraction for Bearing Steels, E2860-12. (2012). https://doi.org/10.1520/E2860.

[20] B.D. Cullity, S.R. Stock, Elements of X-ray diffraction, 3rd edition, Prentice Hall. (2001). https://doi.org/citeulike-article-id:3998040.

[21] ASTM, E8: Standard test methods for tension testing of metallic materials metric, Annu. B. ASTM Stand. 3 (2016) 57–72. https://doi.org/10.1520/E0008.

[22] T. Nicholas, Step loading for very high cycle fatigue, Fatigue Fract. Eng. Mater. Struct. 25 (2002) 861–869.

[23] M. Hinderdael, M. Strantza, D. De Baere, W. Devesse, I. De Graeve, H. Terryn, P. Guillaume, Fatigue performance of Ti-6Al-4V additively manufactured specimens with integrated capillaries of an embedded structural health monitoring system, Materials (Basel). 10 (2017). https://doi.org/10.3390/ma10090993.

[24] O. Andreau, E. Pessard, I. Koutiri, J.D. Penot, C. Dupuy, N. Saintier, P. Peyre, A competition between the contour and hatching zones on the high cycle fatigue behaviour of a 316L stainless steel: Analyzed using X-ray computed tomography, Mater. Sci. Eng. A. 757 (2019) 146–159. https://doi.org/10.1016/j.msea.2019.04.101.

[25] M. Bergant, T. Werner, M. Madia, A. Yawny, U. Zerbst, Short crack propagation analysis and fatigue strength assessment of additively manufactured materials: An application to AISI 316L, Int. J. Fatigue. 151 (2021) 106396. https://doi.org/10.1016/j.ijfatigue.2021.106396.

[26] Y. Ma, P. Feng, J. Zhang, Z. Wu, D. Yu, Energy criteria for machining-induced residual stresses in face milling and their relation with cutting power, Int. J. Adv. Manuf. Technol. 81 (2015) 1023–1032. https://doi.org/10.1007/s00170-015-7278-9.

[27] Y. Li, S. Dong, S. Yan, X. Liu, P. He, B. Xu, Microstructure evolution during laser cladding Fe-Cr

alloy coatings on ductile cast iron, Opt. Laser Technol. 108 (2018) 255–264. https://doi.org/10.1016/j.optlastec.2018.07.004.

[28] J. Grum, R. Šturm, Comparison of measured and calculated thickness of martensite and ledeburite shells around graphite nodules in the hardened layer of nodular iron after laser surface remelting, Appl. Surf. Sci. 187 (2002) 116–123. https://doi.org/10.1016/S0169-4332(01)00823-6.

[29] J.H. Yu, K.Y. Lee, D.S. Shim, S.H. Park, Characterization of mechanical behavior in repaired FC300 using directly deposited AISI-P21 and AISI-H13 metal powders, Proc. Inst. Mech. Eng. Part B J. Eng. Manuf. (2020). https://doi.org/10.1177/0954405419843754.

[30] F. Sciammarella, B. Salehi Najafabadi, Processing Parameter DOE for 316L Using Directed Energy Deposition, J. Manuf. Mater. Process. 2 (2018) 61. https://doi.org/10.3390/jmmp2030061.

[31] Z.E. Tan, J.H.L. Pang, J. Kaminski, H. Pepin, Characterisation of porosity, density, and microstructure of directed energy deposited stainless steel AISI 316L, Addit. Manuf. 25 (2019) 286–296. https://doi.org/10.1016/j.addma.2018.11.014.

[32] B.L. Bramfitt, Structure/Property relationships in irons and steels, ASM Int. (1998) 153–173.

[33] A. Dass, A. Moridi, State of the Art in Directed Energy Deposition: From Additive Manufacturing to Materials Design, Coatings. 9 (2019) 418. https://doi.org/10.3390/coatings9070418.

[34] R.P. Martukanitz, Directed-Energy Deposition Processes, Addit. Manuf. Process. 24 (2020) 220–238. https://doi.org/10.31399/asm.hb.v24.a0006549.

[35] H. Gong, K. Rafi, H. Gu, T. Starr, B. Stucker, Analysis of defect generation in Ti-6Al-4V parts made using powder bed fusion additive manufacturing processes, Addit. Manuf. 1 (2014) 87–98. https://doi.org/10.1016/j.addma.2014.08.002.

[36] H. Zhang, D. Gu, J. Yang, D. Dai, T. Zhao, C. Hong, A. Gasser, R. Poprawe, Selective laser melting of rare earth element Sc modified aluminum alloy: Thermodynamics of precipitation behavior and its influence on mechanical properties, Addit. Manuf. 23 (2018) 1–12. https://doi.org/10.1016/j.addma.2018.07.002.